Advanced Electronic Materials

ADVANCED ELECTRONIC MATERIALS Open Access

www.advelectronicmat.de

RESEARCH ARTICLE OPEN ACCESS

Cement-SnSe Thermoelectric Devices With High Seebeck Coefficients

Geraint Howells[1] | Shahin Mehraban[2] | Thomas Dunlop[3] | Nick Lavery[2] | Matthew J. Carnie[4] | Matthew Burton[4]

[1]Department of Materials Science & Engineering, Faculty of Science and Engineering, Swansea University, Swansea, UK | [2]Materials Advanced Characterization Centre, Faculty of Science and Engineering, Swansea University, Swansea, UK | [3]Advanced Imaging Materials, Faculty of Science and Engineering, Swansea University, Swansea, UK | [4]SPECIFIC-IKC, Department of Materials Science & Engineering, Faculty of Science and Engineering, Swansea University, Swansea, UK

Correspondence: Geraint Howells (829468@swansea.ac.uk) | Matthew Burton (Matthew.burton@materials.ox.ac.uk)

Received: 17 September 2025 | **Revised:** 21 November 2025 | **Accepted:** 1 December 2025

Keywords: cement | SnSe | thermoelectrics | tin selenide

ABSTRACT

In this work, we present a cost-effective, scalable approach for fabricating thermoelectric (TE) generators using p-type tin selenide (SnSe) bonded in a cement matrix via a slurry mold casting technique. Traditional methods for manufacturing SnSe-based TE materials are energy-intensive and economically unfeasible. By contrast, our approach employs common Portland cement as a binder, offering a viable alternative that reduces processing time, complexity, and cost. Ball-milled SnSe is mixed with varying concentrations of cement and cast into molds for samples, resulting in dimensions of $1.5 \times 1.5 \times 0.75$ cm^3. The best-performing formulations are 0.2 wt.% cement, which exhibited a power factor of 77 μW m^{-1}·K^{-2} at 800 K and the 0.3 wt.% cement sample, which has a peak ZT of 0.3 at 850 K, the highest ZT of any cement containing TE to date. A proof-of-concept thermoelectric generator (TEG) comprising six legs of SnSe-cement composite demonstrated a peak power output of ~73 μW at 850 K. Furthermore, calculations show that using the cement-bonded SnSe to harvest industrial waste heat in a steel-making environment can yield a potential 1521.3 W m^{-2} of electrical energy.

1 | Introduction

The increasing pressure to alleviate the use of fossil fuels for energy usage has meant there is a need to use greener, more sustainable methods of energy production [1–3]. These methods include solar cells, wind energy, and hydropower. These, however, rely on external stimuli such as the sun, wind, and a reliable quantity of water, respectively. Another method of sustainable electricity production that can be utilized is thermoelectric generators (TEGs) [4–7]. TEGs produce electrical energy by taking advantage of a heat differential that is applied across the thermoelectric (TE) material [8, 9]. They have the potential to be used in areas where waste heat is produced, and a 2014 study found that from UK industry alone, 48 TWh yr^{-1} of energy is lost as waste heat [10]. They work by utilizing the Seebeck effect, where a movement of charge carriers occurs from the high-energy hot side to the low-energy cool side [11]. There are two types of TE materials, p-type and n-type, which have holes and electrons as charge carriers, respectively. TEGs consist of alternating p-type and n-type legs, which are connected electrically in series and thermally in parallel. The performance of TE materials is characterized by the dimensionless figure of merit (ZT), which consists of the Seebeck coefficient (S, V K^{-1}), electrical conductivity (σ, S m^{-1}), thermal conductivity (κ, W m^{-1} K^{-1}), and the absolute temperature (T, K), as shown in Equation 1 [12].

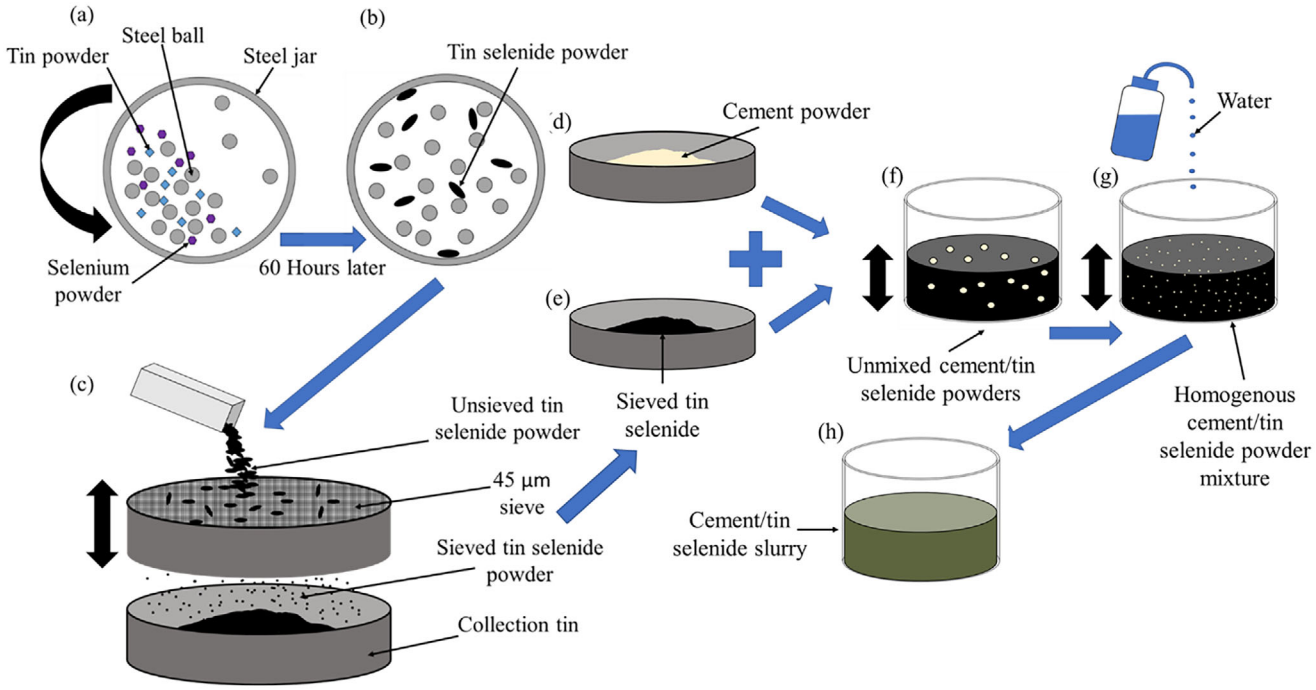

FIGURE 1 | This diagram illustrates the process of ball milling and slurry production, with thick black arrows indicating the various movements involved. The steps involved are as follows: (a) the initial stage before ball milling, (b) the process after ball milling, (c) the resulting tin selenide powder is sieved, (d) cement powder is obtained, (e) the tin selenide powder obtained from step (c) is mixed with the cement powder, (f) the mixture is turned into an unmixed slurry, (g) which is then agitated and (h) ultimately results in the final cement/tin selenide slurry [61].

$$zT = \frac{S^2\sigma}{\kappa}\,T \tag{1}$$

In the 1950's bismuth telluride (Bi_2Te_3) was found to have a ZT of ~1, and since then, the compound and its doped derivatives (Se for n-type, Sb for p-type) have become the most researched TE material [13–16]. Bi_2Te_3, however, is only effective at low temperatures (400–600 K), so lead telluride (PbTe) must be employed for medium temperatures (600–900 K). PbTe and its derivative compounds were found to be more efficient at these temperatures, with Fu et al. achieving a ZT of ~2.2 at 820 K using $PbTe_{0.8}Se_{0.2}$ with 8% MgTe [17]. Although these ZT numbers are deemed high enough to manufacture commercially viable TEGs materials that have efficiencies comparable to those of other green technologies [18], they are all telluride compounds, which is a relatively rare element on Earth, with a similar abundance to Pt (1 μg kg^{-1}) [19, 20]. Subsequently, if these materials were to be widely adopted in industry, the cost of tellurium would become economically unsustainable. The toxicity of tellurium is also a great concern [20]. As a result of these issues, new materials must be used for TE applications [11]. One such candidate that has recently been investigated is tin selenide (SnSe) [21–36]. SnSe is a promising material for TE applications due to its favorable Seebeck coefficient and low thermal conductivity. The low thermal conductivity (κ [$\kappa = \kappa_e + \kappa_L$]) [37] is attributed to the low lattice component, κ_L, which is the result of the spring-shaped structure down the b and c axes of the crystal structure. The detection of a high ZT value of 2.6 in single crystals of SnSe accelerated this interest in its potential as a TE material [38]. In 2021, polycrystalline SnSe was found to have a ZT value even higher than that of a single crystal, with Zhou et al. achieving a ZT of 3.1 at ~783 K, the highest ZT recorded to date [39].

The aforementioned SnSe was obtained using energy-intensive manufacturing methods, which makes them costly to manufacture, thus making them commercially unattractive. For instance, the production of single-crystal SnSe involves Bridgeman crystal growth, which requires specialist equipment, high temperatures (>1200 K), and long manufacturing times [38, 40]. Similarly, the production of polycrystalline SnSe requires high temperatures and the use of typical techniques such as spark plasma sintering (SPS), which is also an energy-intensive process. These techniques are not just tied to SnSe, with the Bi_2Te_3 compounds also using SPS and hot press sintering [41]. The inherent cost associated with these established methods also contributes to the increased cost of TE energy ($0.80 per kWh), which is an order of magnitude higher than photovoltaic and wind turbines ($0.089, and $0.084 per kWh, respectively) [9, 42]. Alternative methods for making TEGs, therefore, need to be investigated. One such method is printing.

Printing can be done without specialist equipment, at ambient temperature and pressure, and is easily scalable. Most printing of TE materials has concentrated on screen printing [43], and in 2018, Han et al. achieved a ZT of >1 at 623 K, albeit with PbTe compounds [44]. Other techniques include inkjet [45] and dispenser printing [46–48]; however, all end products of these techniques show an unsuitable thickness (<1 mm) for TEG use (where >5 mm is typically required). Printing of SnSe has been investigated before by Burton et al. This involved a pseudo 3D printing technique using a cellulose-based binder, yielding a ZT of 1.7 [9, 23], a record for printed TEs. The manufacturing times, however, were too long for the technique to become commercially viable. Here, we investigate the feasibility and performance of

using construction cement as a binder for ball-milled SnSe, using a method akin to traditional concrete casting, which could potentially dramatically cut the cost to produce TEGs. Cement is a long-established binder for concrete composites (along with rock aggregate) [49], and concrete itself has been investigated before for potential TE applications by the contribution of additives to the concrete matrix. These, however, have mostly been limited to carbon or metal oxide-based TEs, and result in generally low ZT values when compared to traditionally made TEs [50–59]. The potential practical use of cement for TE composites has seen recent improvements however, Wei et al. investigated the feasibility and usefulness of TE concrete in 2021 and calculated that 35.2 kWh of power could be harvested from a road of 1 km in 8 h made from TE concrete (Zinc oxide [ZnO] additives), which also equates to a power production of 440 mW m^{-2} [60]. In contrast, this work is the first to incorporate SnSe, a leading p-type chalcogenide TE, into a cement binder. Here, SnSe serves as the primary TE material, with cement acting only as the structural binder. This produces a castable SnSe-cement composite TEG element, representing the first use of cement as a processing route for SnSe TEs.

2 | Experimental

2.1 | Ball Milling

Mechanical alloying of the raw elements of Sn and Se was achieved via ball milling. Sn (≥99%, Sigma–Aldrich) and Se (≥99.5%, Sigma–Aldrich) were added in equal molar quantities into a stainless-steel jar with 30 stainless-steel ball bearings (10 mm diameter). Another jar was loaded with the same contents to allow the mill to be balanced. The jars were then secured in a planetary ball mill (PULVERISETTE 5/2), and a spin speed and time of 200 rpm and 30 min were used, respectively, followed by a 30 min rest period. This was repeated 60 times, giving a total ball milling time of 60 h. After each spin cycle, the spin direction was reversed. The ball-milled powder was then sieved in a 45 μm sieve (Endecotts) to ensure all SnSe particles were 45 μm or below (Figure 1).

2.2 | Slurry Mold Casting

Portland construction cement powder (Blue Circle Mastercrete) was mixed in with the ball-milled SnSe powder and agitated using a vortex genie to ensure a homogenous powder mixture. The addition of cement powder resulted in 6 different sample formulations of 0.1%, 0.2%, 0.3%, 0.4%, and 0.5% by weight of cement. Each of the powder mixtures had an amount of deionized water added to it that equalled a quarter of the mass of the SnSe powder. The resulting slurry was agitated in a vortex genie until no solids were visible and the mix was uniform. The slurry was then poured into a silicon mold until it was three-quarters full and left to dry overnight, as seen in Figure 2. The samples were then removed and measured approximately 1.5 cm × 1.5 cm × 0.75 cm. The samples were then cured in an Ar tube furnace for 1 h at 873 K with an Ar flow rate of 1 L min^{-1}, after which the furnace heating coil was turned off, allowing the samples to cool to room temperature.

2.3 | Material Characterization

XRD was performed on a Brucker D8 diffractor with Cu Kα radiation. Scanning electron microscopy (SEM) and energy-dispersive X-ray spectroscopy (EDX) were performed on a Joel 7800F field emission gun (FEG) SEM with an Oxford Laboratory EDX attachment. X-ray photoelectron spectroscopy (XPS) was performed on a Kratos Axis Supra instrument, and data were processed in CasaXPS (2.3.24PR1.0). Samples were mounted in electrical contact with the stage. XPS sampled to a depth of <10 nm using a monochromatic Kα source (225 W, 15 mA) with a footprint 300 μm × 700 μm and a pass energy of 40 eV, with the GL(30) lineshape.

2.4 | Thermoelectric Characterization

Electrical conductivity and Seebeck coefficients were measured in a He atmosphere using an ULVAC ZEM3. Uncertainty of electrical conductivity ±3% and Seebeck coefficients ±4% [62]. Thermal diffusivities (D) were determined using a Netzsch 457 laser flash analyser (LFA) with Al_2TiO_5 sample holders with SiC caps for solid samples, Ø 11 mm × 1.5 mm, and using the Cowon + pulse correction diffusivity model. This was calibrated with a 10 mm Ø Pyroceram 9606 calibration standard. The uncertainty of thermal diffusivity is ±3% [62]. Densities were determined using the method of hydrostatic weighing that uses Archimedes' principle, with results reported in Table S2. The dimensions were measured before and after measurement, with no observable changes. Uncertainty in density measurements is ±1% [62].

3 | Results and Discussion

3.1 | Characterization of Materials

Figure 3a shows the XRD spectra for commercially made SnSe, ball-milled SnSe, the 0.1% cement sample (post-cure), the starting powders, and a pure cement sample with no SnSe. The initial peaks from the Sn and Se powders disappear once ball-milled, and the resulting ball-milled XRD peaks match the commercially made SnSe. Both observations indicate that there is negligible or no constituent powder left after ball milling, and that they have been formed into SnSe via a solid-state reaction. The XRD pattern of samples containing ball-milled SnSe and cement binder exhibits similarities to our previous work [61], with a prominent peak at approximately 32° corresponding to the (1 1 1) plane. XRD analysis of a pure cement sample (Figure 3a) demonstrates that the same peaks are observed when combined with SnSe, indicating the absence of chemical reactions between SnSe and cement upon their combination. XRD spectra for the pre-cured (Figure 3b) and post-cured (Figure 3c) samples reveal that curing in an argon environment results in narrower and taller peaks, indicating grain growth across all binder concentrations. The Scherrer equation, assuming spherical particles, was employed to calculate the extent of grain growth. Figure 3d illustrates a general trend of grain growth after curing.

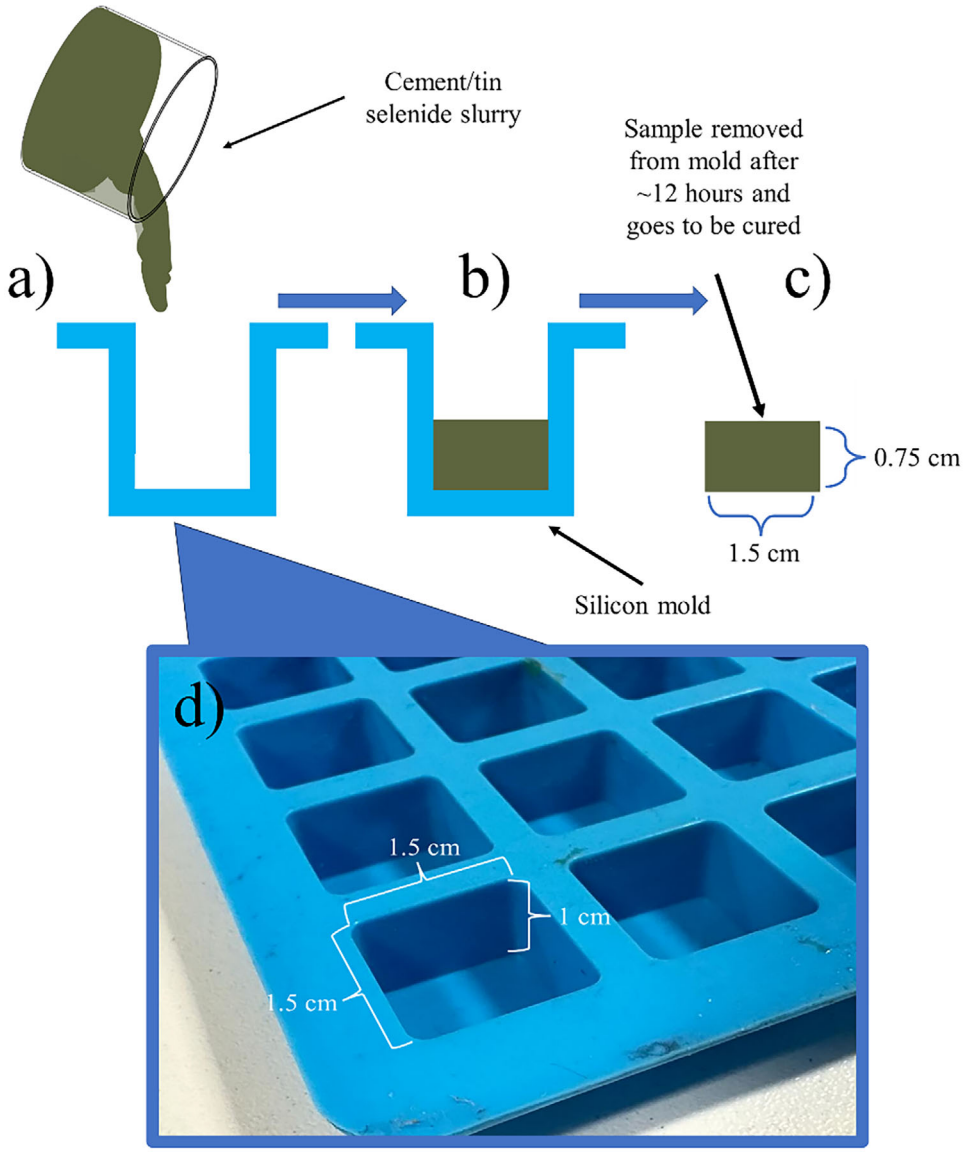

FIGURE 2 | This diagram illustrates the casting process, where the pour is seen in (a), and the slurry is poured until the mold is filled, (b), and then is removed from the mold, c).

Much like our previous work on Na_2SiO_3 [61], chemical state assignment for tin can be difficult, as there are overlapping 3d 5/2 values for SnO_2 and SnO. Furthermore, both of these are close to the Sn metal peak. In Figure 4a, the first peak is at approximately 485.6 eV, which is closely associated with the tin metal peak, Sn 3d 5/2. The second peak for 3d 5/2 values is at approximately 486.8 eV, which resembles the peak for Sn 3d SnO_2 5/2. There are also two peaks for the Sn 3d 3/2 region. The first peak is at approximately 493.5 eV, which is associated with the peak for Sn 3d metal 3/2. The second peak in this region is at 495.2 eV, which is the Sn 3d SnO_2 3/2 peak. This shows that on the surface at least, there are oxidation products present. Unlike our previous work, though on Na_2SiO_3, the Sn peaks, for 3/2 and 5/2, each have a double peak, with each peak representing Sn oxide products or Sn metal. This double peak for each region was not present in the previous XPS analysis on Na_2SiO_3 [61]. Figure 4b shows the XPS Se spectra, cured. There is a peak at 53.7 eV, which resembles the peak for Se in the previous work on Na_2SiO_3.

Figure 4c shows the XPS spectra for the Ca, cured. Ca was selected for analysis as it is present in the cement binder in large amounts. There are two peaks present in the Ca XPS spectra, the first is at approximately 347.1 eV, which is the Ca 2p 3/2 peak. The second peak is at approximately 350 eV, which is the Ca 2p 1/2 peak. Both peaks are associated with $CaCO_3$. $CaCO_3$ (calcium carbonate) is the main form of calcium within cement. It helps to accelerate the curing rate of concrete and increases the cement's slump rate. Si is also within cement, and although not shown here, it was detected by the XPS (Figure S3). The spectra for Si are seen in our previous work on Na_2SiO_3 [61], and there was no discernible difference between the two XPS spectra.

Figure 4e,f display the 0.1% and 0.5% formulations using Scanning Electron Microscopy (SEM). Supplementary information, specifically Figure S4, includes additional SEM images of the remaining formulations. It was observed that all the samples examined exhibited no particles greater than 45 μm in size,

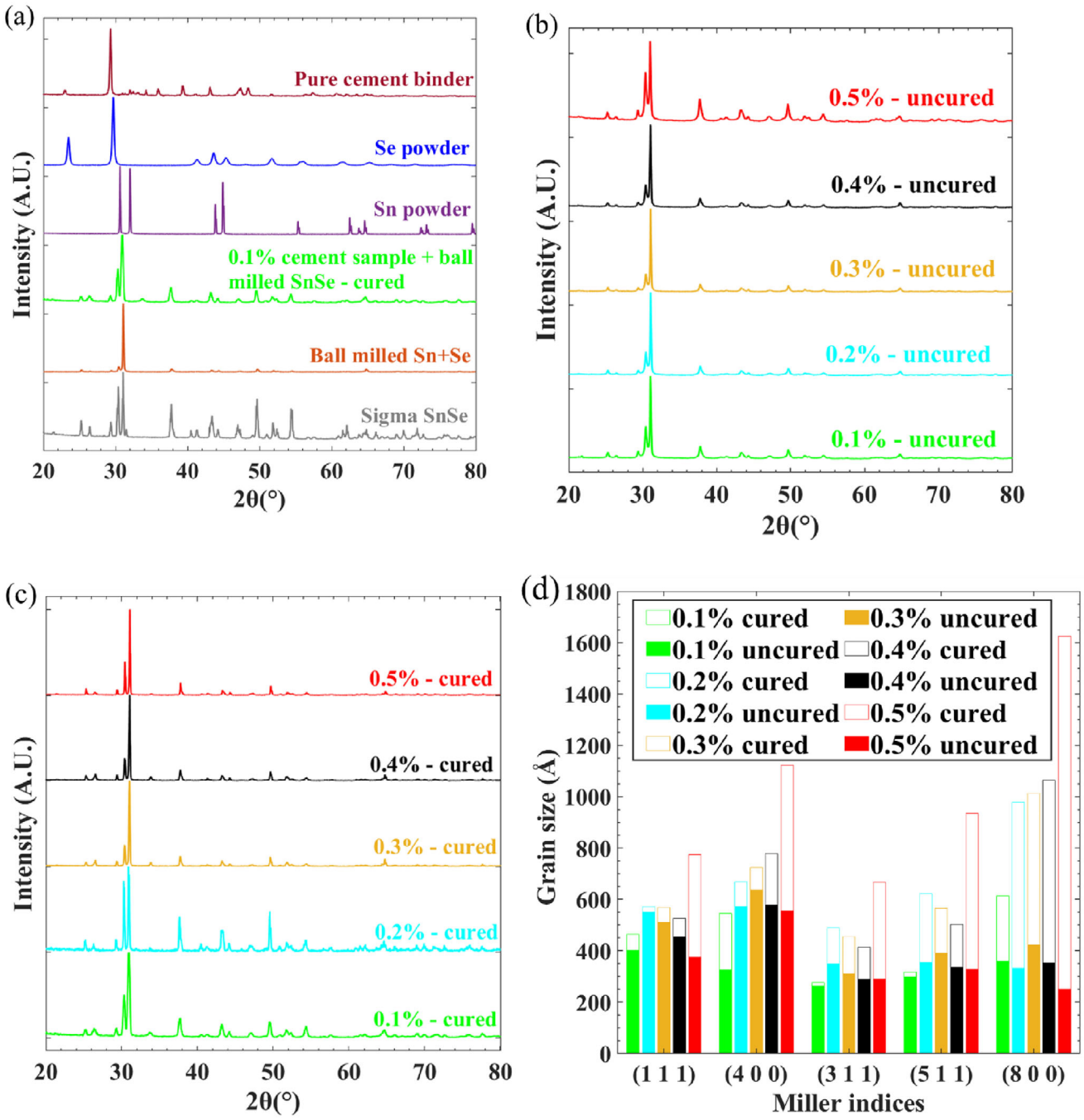

FIGURE 3 | XRD: (a) constituent materials, ball-milled SnSe and commercially available SnSe, (b) uncured samples, (c) cured samples, and (d) grain growth of samples, full bars represent samples before curing, whereas line bars represent samples after curing.

which aligns with expectations from the sieving process carried out following ball milling. The surface of all samples displayed varying degrees of porosity post-curing, with the highest degree of porosity present in the 0.1% sample. It is also worth noting that this lack of coalescence in the 0.1% sample could also be observed by eye, as it appeared slightly powdery, demonstrating the lack of cement binder. This porosity can also be observed in the density measurements of the samples (Table S2), with the average density of these cement-bonded samples (3.99 g cm^{-3}) being significantly less than that of our previous work (5.3 g cm^{-3}) [61] and the theoretical density of SnSe (6.18 g cm^{-3}).

Energy-dispersive X-ray spectroscopy (EDX) was also conducted on the surface of the samples for bulk composition analysis; these showed excess oxidation, and a substantial excess for tin (~>65:35 atomic ratio with Sn excess). As a result, a small scratch was made on the sample surface (Figure S4e), and EDX was conducted on the scratched area. Atomic weight percentages are shown in Figure 4d for the scratched surface EDX. All samples still show excess Sn; however, these numbers are still aligned with our previous findings that EDX analysis of a commercially sourced SnSe powder (Sigma–Aldrich, 99.995%) indicates a 60:40 atomic% weighting toward Sn over Se [24]. This indicates that

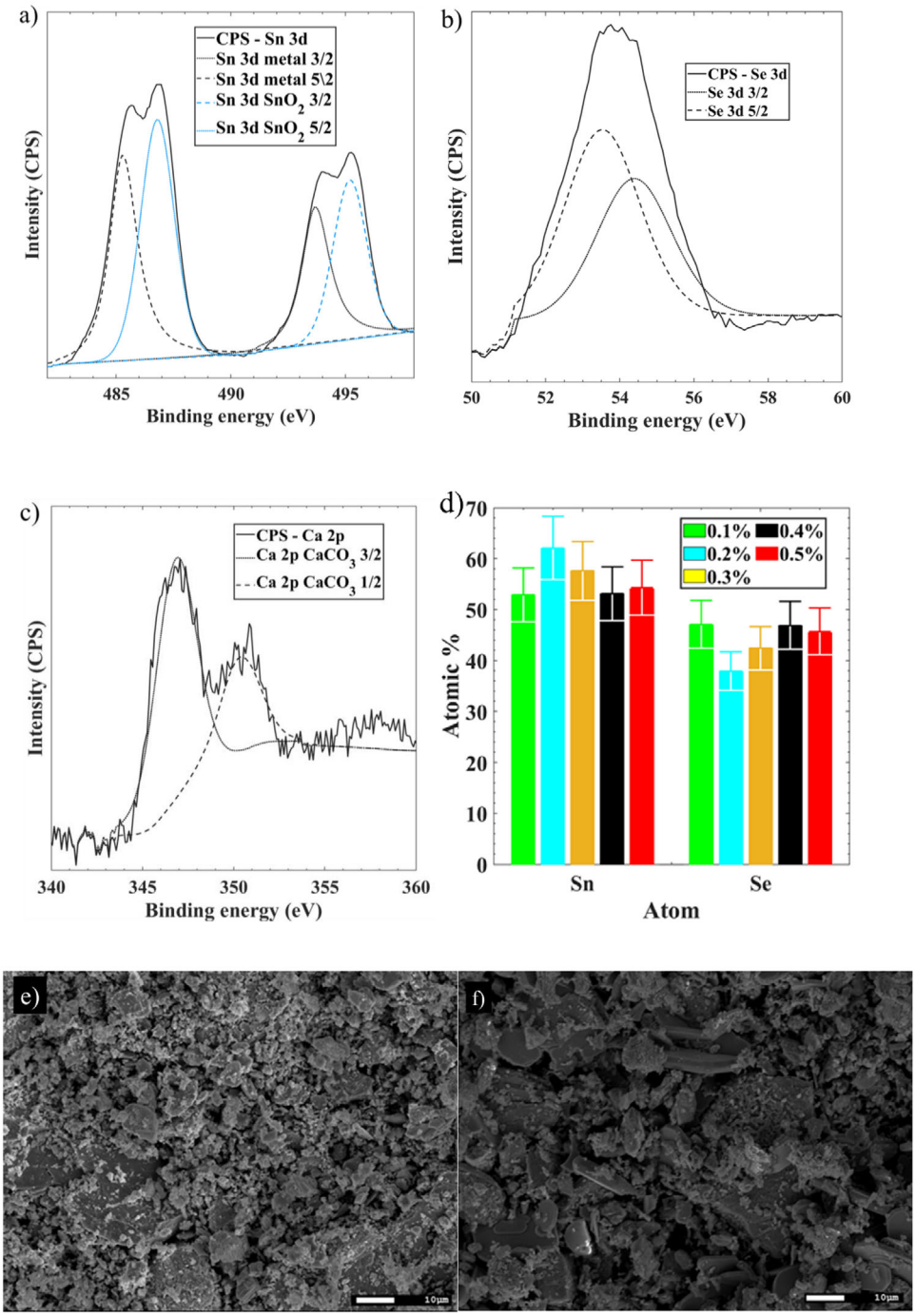

FIGURE 4 | (a) Sn XPS spectra of the cured 0.1% cement sample, (b) Se XPS spectra of the cured 0.1% cement sample, (c) Ca XPS spectra of the cured 0.1% cement sample, (d) EDS atomic weights of made samples, (e) 0.1% cement cured SEM image, (f), −.5% cement cured SEM image.

the reason for our observed Sn excess could be an issue with an error in our spectrometer, or a partial loss of Se upon annealing that was observed by Zainal et al., [63]. The stark lack of Se on the surface of the samples indicates that, again, much like within our previous work, Se evaporates from the surface of the samples during annealing, but within the bulk of the sample, the Se has remained mainly in place. EDX atomic weight percentages for the non-scratched surface are available in the supporting information, Table S1.

3.2 | Thermoelectric Characterization

Figure 5a displays the electrical conductivity of the samples. Electrical conductivity increases with decreasing amounts of cement, down to a cement concentration of 0.2%, where it hits a peak of 5.44 S cm^{-1} on its second run. This is because, as the cement amount decreases, there are fewer insulating barriers that block the path of electrical pathways within the material. At the lowest cement concentration, however, the electrical

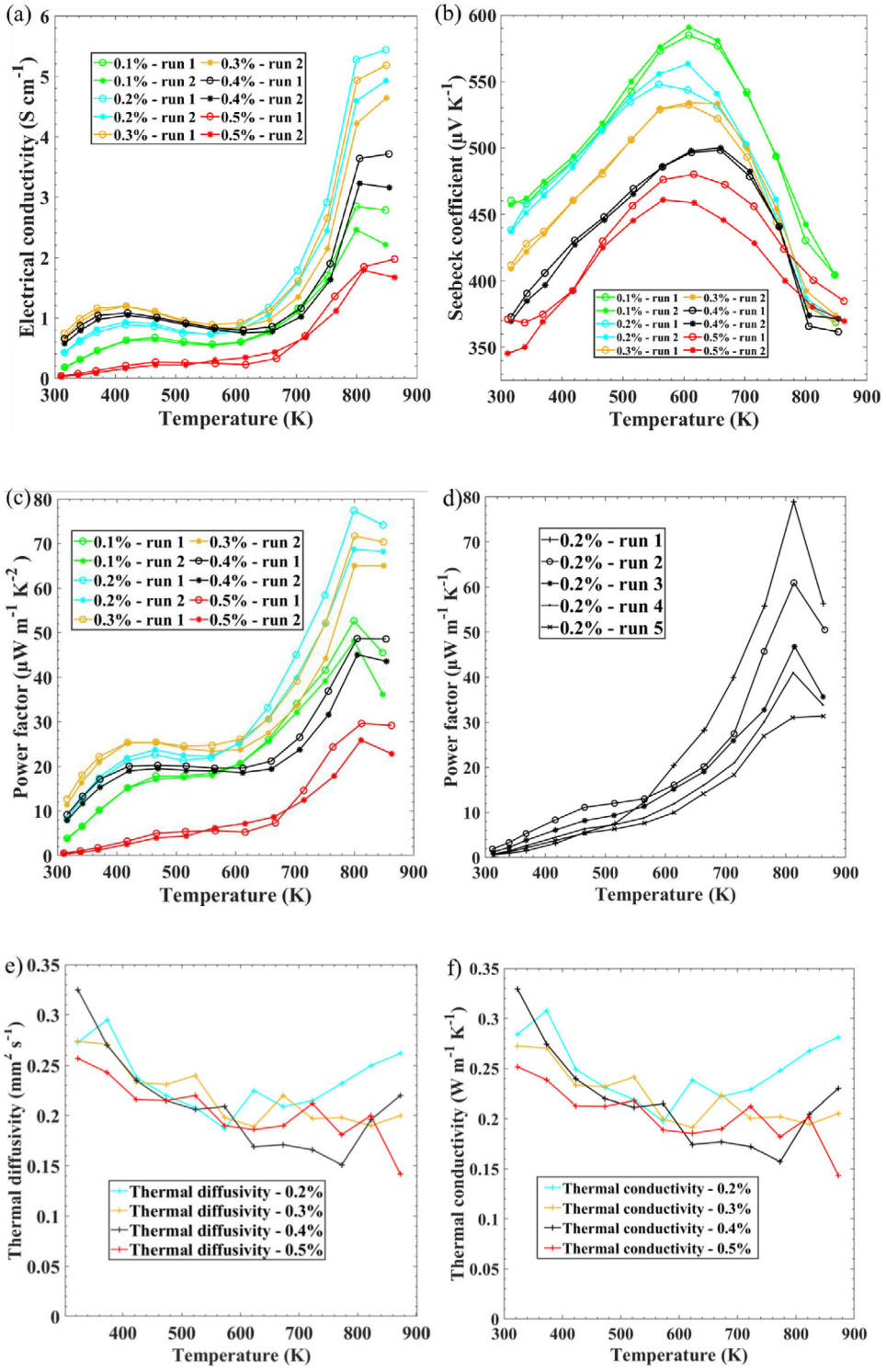

FIGURE 5 | TE performance of Cement-SnSe composites (circular marks represent the first runs, while the star marks represent the second runs): (a) electrical conductivity, (b) Seebeck coefficient, (c) power factor, (d) power factor of long-term thermal cycling, (e) thermal diffusivity, and (f) thermal conductivity.

conductivity decreases back down to levels comparable to the higher percentage cement content (~3 S cm^{-1}). This is because at the lowest cement concentration, there is insufficient coalescence within the SnSe particles for electron pathways to occur, resulting in the drop of electrical conductivity. This lack of coalescence can be seen within the aforementioned SEM image (Figure 4e).

The general trend of electrical conductivity follows that of our previous work [61], with an initial rise, a subsequent drop (~600 K) and a final, higher peak at ~873 K. This behavior can be explained by the phase change that SnSe undergoes at ~750 K, where it goes from a layered, orthorhombic Pnma, which can be described as a distorted rock salt structure to a higher

symmetry Cmcm structure [64, 65]. This Cmcm structure is more electrically conductive than the Pnma phase, hence the higher electrical conductivity exhibited at higher temperatures. It is worth noting that the amount of cement binder within the different samples did not affect conductivity to the same magnitude as our previous work on Na_2SiO_3 [61]. The Seebeck coefficient results are seen in Figure 5b. The Seebeck coefficient trend is similar to previous work completed on SnSe [23, 61], such as those using carboxy-methyl-cellulose or Na_2SiO_3 binders; with a rise in Seebeck coefficient from room temperature before hitting a peak at ~600 K, before a decline at higher temperatures. This decline in Seebeck coefficient is again explained by the phase change SnSe undergoes at higher temperatures. The largest Seebeck coefficient is seen in the 0.1% sample, hitting peaks 584 μV K^{-1} and 590 μV K^{-1} on the first and second thermal ZEM3 cycle at ~610 K. The magnitude of the Seebeck coefficient observed in the samples is negatively affected by binder concentration, with 0.5% showing the lowest Seebeck peaks, of 476 μV K^{-1} and 460 μV K^{-1}, both observed at ~600 K.

The observation of decreasing Seebeck coefficient with increasing binder is due to the cement interfering with the SnSe mechanisms, which produced the Seebeck effect, due to the cement being n-type [66–69]. This possible effect was investigated further by making a sample with 10% by weight of cement, as seen in Figure 6a. This sample was n-type along most of the thermal cycling, up to approximately 800 K, where it switches to p-type. The peak magnitude of the n-type Seebeck coefficient was −133 μV K^{-1} at 500 K on the second thermal cycle. Although Hall effect measurements were not performed due to lack of access to the required equipment, the n- to p-type transition observed at 10% cement content is consistent with ionic TE behavior reported in cement pastes, where OH^- leaching and subsequent Ca^{2+}, Na^+, and K^+ migration lead to a temperature-dependent polarity reversal. While this interpretation is partly speculative, the agreement with published cement ionic mechanisms and the reduction in Seebeck magnitude with increasing cement content suggest that the polarity change originates from ionic charge transport within the cement matrix [67, 70, 71]. Power factor results are seen in Figure 5c, where the highest power factor was shown by the 0.2% sample, hitting a peak of 77 μW m^{-1} K^{-2} at 800 K.

As the 0.2% cement-SnSe exhibited the highest power factor, the reproducibility and thermal hysteresis were tested with that concentration of the binder with a new sample. Five thermal cycles from RT to 850 K were conducted. The power factor (5d) decreased to 31.4 μW m^{-1} K^{-2} at ~850 K after five thermal cycles; this is likely due to the continued breakdown of the cement binder through thermal cycles, although a visual inspection was done after thermal cycling, and no cracks or defects were noted, a mechanical and cyclic durability study will be carried out in future work.

The thermal conductivity of the samples, Figure 5f, was determined through the product of the thermal diffusivity (Figure 5e), density (Table S2), and specific heat capacity obtained from literature. All values observed are in the range of ~0.32 to ~0.14 W m^{-1} K^{-1}, with an inverse correlation with the measurement temperature. These numbers are in line with those seen for the *a*-axis of single-crystal SnSe and lower than those seen for the *b*-axis and *c*-axis. The 0.4% sample and the 0.5% sample produced the highest and lowest thermal conductivity values, respectively, although this difference is within the experimental error. Similar to our previous work utilizing a Na_2SiO_3 binder [61], there is no obvious trend between thermal conductivity and binder concentration. Thermal conductivity of the 0.1% sample was not measured, as the powdery surface of the sample was seen as a danger to the LFA equipment. The density, as mentioned earlier, was lower than that of our previous work on Na_2SiO_3 [61]. While denser TE materials generally promote higher electrical conductivity, the reduced density of the cement-SnSe composites can also be advantageous. The increased porosity helps to suppress lattice thermal conductivity through enhanced phonon scattering, which contributes to the low thermal conductivity values observed. However, excessive porosity can also limit charge-carrier transport between SnSe grains and reduce electrical conductivity.

A peak ZT (Figure 6a) value of 0.3 is seen at 823 K by the 0.3% sample, a value which is the highest for cement containing TE materials, with values seen in Figure 6c [50–55, 59, 60].

3.3 | Thermoelectric Generator

A proof of concept, p-type only TEG was made. To achieve this, six SnSe legs were made using the 0.2% cement content, as this had the highest power factor. The six legs were then connected in a Z-type connection. A schematic and an image of the setup are seen in Figure 7a,b, respectively. A hot plate was used as the heat source, with no active cooling utilized. A thermocouple was used to measure the hot (T_H, K) and cold (T_C, K) temperatures, with a multi-meter measuring the short-circuit current (I_{SC}) and open-circuit voltage (V_{OC}). Peak power output of the device was calculated assuming that maximum power = $I_{SC}V_{OC}/4$ [72]. For the connection between the legs, copper tape was used, and to alleviate parasitic contact resistance [73], silver paint was utilized as a glue between the copper tape—SnSe interface. Silver paint was used as the contact material due to its low resistance, availability, and ease of use for a proof-of-concept device, and has been proven effective in previous work [61]. While nickel offers improved thermal stability, it requires additional high-temperature or sputtered processing steps and so was not considered for this TEG.

The TEG performance was measured in both directions of casting, with the legs laid down, so casting direction is parallel to the heat source, and perpendicular to casting with legs upright on the heat source. Full TEG data for both directions is available in Table S3. The voltage generated by the TEG demonstrates a rapid increase as the temperature rises from room temperature for both samples, Figure 7c. At 593 K, the perpendicular TEG reaches an initial peak of 603 mV, whereas the parallel TEG shows a peak of 251 mV at the same temperature. Subsequently, both TEGs experience a decline in voltage as the SnSe undergoes a phase transition from Pnma to Cmcm. Nonetheless, both TEGs display subsequent voltage peaks toward 850 K, measuring 592 and 482 mV for the perpendicular and parallel heated TEGs, respectively. This voltage pattern aligns with the observations made in the Seebeck coefficient results obtained from the ZEM3. The current for both TEGs is illustrated in Figure 7d. The current

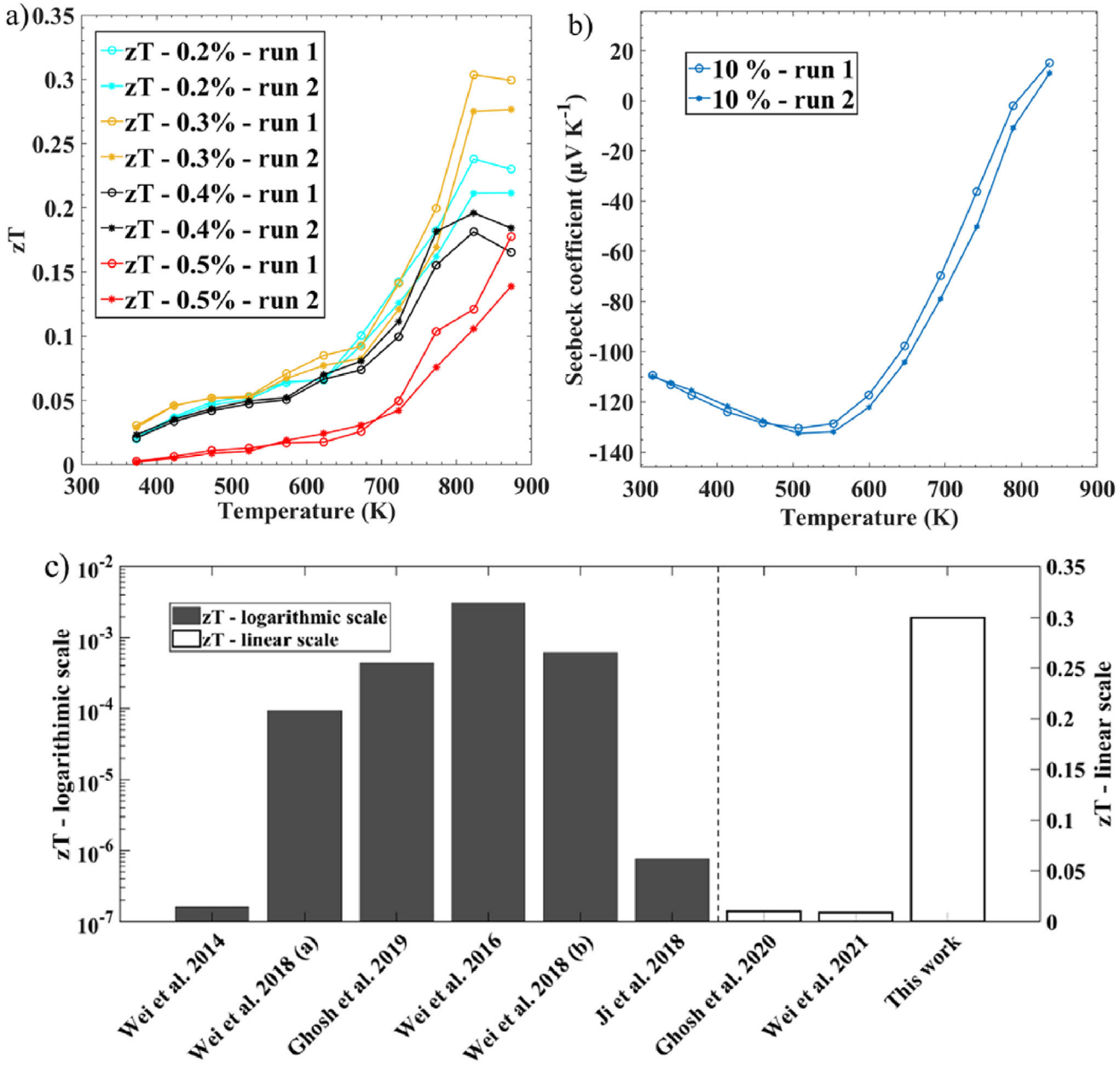

FIGURE 6 | (a) ZT of the cement-SnSe samples, (b) the Seebeck coefficient of the 10% by weight cement sample (n-type), and (c) ZT values of cement containing thermoelectrics, with values taken from [50–55, 59, 60].

for both TEGs, at first, gradually increases as the temperature rises, before both significantly rise after 600 K. The parallel TEG, however, hits a significantly higher peak of 605 μA, compared to 142 μA exhibited by the perpendicular TEG. This pattern, much like the voltage, aligns with the results obtained in the ZEM3, where these materials show the highest conductivity at the higher testing temperatures. Power output for both TEGs is shown in Figure 7e. The parallel TEGs show a peak power output of ~73 μW compared to ~21 μW produced by the perpendicular TEGs.

It is worth noting that the TEG heated perpendicular to casting exhibits a significantly higher voltage output, but lower current compared to the parallel heated TEG. Two possible reasons could account for this. First, placing the TEGs perpendicular to the heat source increases the distance between the hot and cold sides, resulting in a larger temperature difference (ΔT) within the TEG [74]. The voltage produced by the TEGs is proportional to this ΔT value, as seen in Equation 2, where ΔV is the voltage produced (V, sometimes expressed as −V), S is the Seebeck coefficient (μV K^{-1}), and T is the temperature (K) [67, 75]. The ΔT data from both TEGs in Table S4 support this, where the perpendicular TEG has a higher ΔT than the parallel TEG.

$$\Delta V = S\Delta T \tag{2}$$

When the TEGs are laid flat, however, more surface area and thus more TEG volume is exposed to the heat source, and so more charge carriers within the SnSe lattice can undergo thermal excitation up to the conduction band, increasing charge

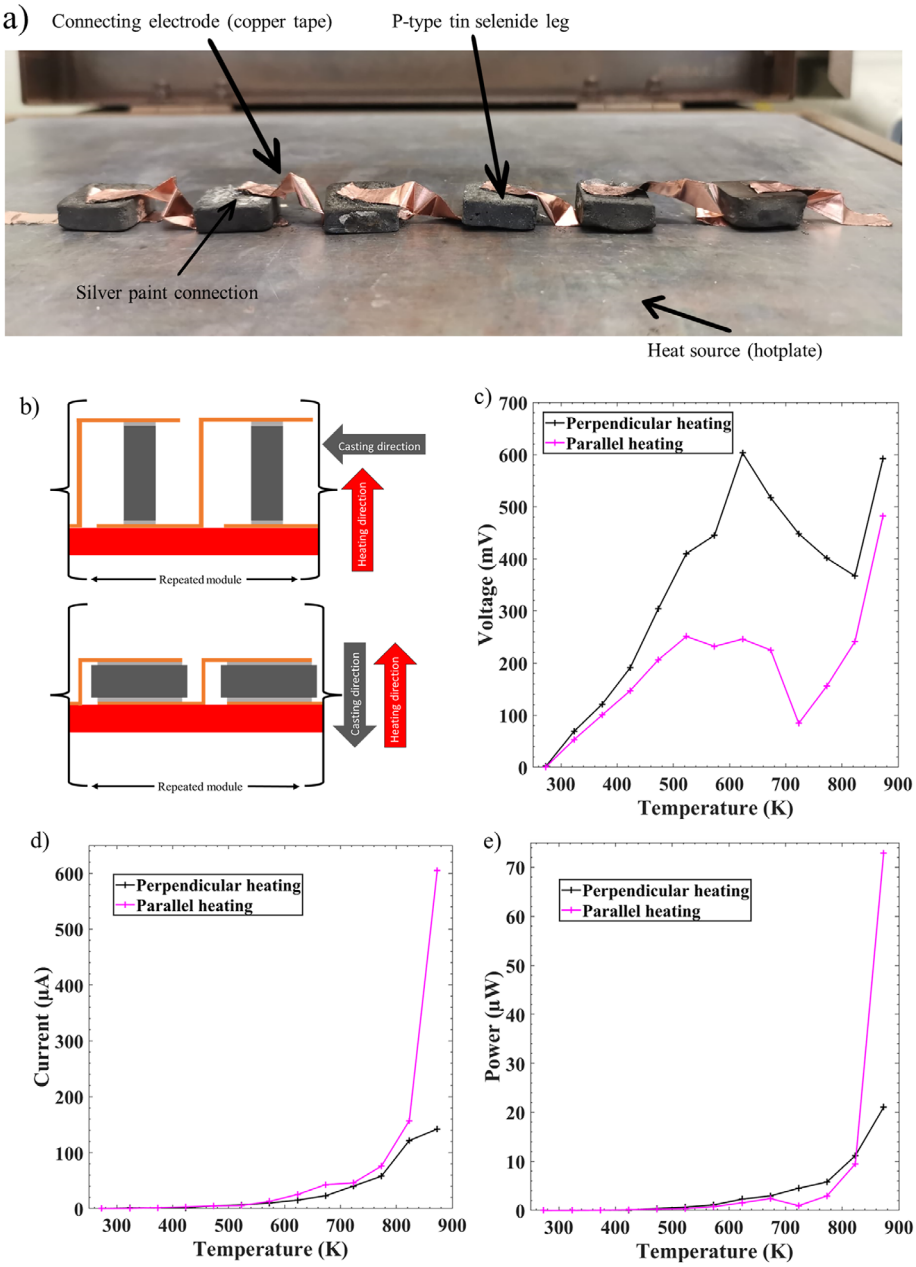

FIGURE 7 | (a) Photo of the TEG during parallel heating, (b) illustration of the TEG testing setup, (c) open-circuit voltage (V_{OC}) output of TEGs, (d) short-circuit current (I_{SC}) output of the TEGs, and (e) peak power output of the TEGs (maximum power = $I_{SC}V_{OC}/4$) [64].

carrier mobility. Increasing charge carrier mobility has an effect on where these charge carriers end up transporting heat (κ_e) throughout the TEG, too. This transport of heat from the hot side to the cooler side is detrimental to the ΔT portion of Equation 2, thus lowering the voltage.

Second, as leg length increases, the pathway length for holes to travel from the hot side to the cold side also increases. As the holes move through the TEG, they experience resistance due to scattering events and interactions with the lattice structure. With a longer path, the holes have more opportunities to undergo multiple scattering events, which can result in a larger voltage potential being built up along the leg, leading to a higher voltage output due to the increased resistance. In contrast, when the TEGs are laid flat, the leg length is decreased, reducing the overall resistance and facilitating a smoother flow of current within the parallel sample, but lower voltage. This lower voltage, however, does not offset the rise in current, hence the higher power in the parallel TEG. Although SnSe crystals are intrinsically anisotropic, the polycrystalline cement-SnSe composites used here have random grain orientation and therefore behave isotropically. The variation between the perpendicular and parallel TEG configurations (Figure 7c–e) arises from how heat interacts with the geometry of the device rather than from crystallographic effects. The perpendicular configuration produces a higher temperature gradient across each leg, resulting in greater voltage, while the parallel configuration exposes more SnSe volume to the heat, increasing current output.

Using the same calculations that Wei et al. used for their power output (35.2 kWh or 440 mW m^{-2}) from a road of 1 km by 10 m [60] would yield a lower yet comparable result of 26 kWh or 325.8 mW m^{-2} using a Seebeck of 437 μV K^{-1} and electrical conductivity of 0.43 S cm^{-1}. This, however, is at a ΔT that is not optimal for SnSe. To better reflect conditions where SnSe performs more efficiently, such as in steelmaking environments where operating temperatures on average can reach 800 K, the calculation can be adjusted accordingly. At 800 K, SnSe exhibits improved TE properties, with a Seebeck coefficient of 372 μV·K^{-1} and electrical conductivity of 5.4 S·cm^{-1}. Assuming a similar, average ΔT of ∼800 K across refractory linings such as the ones found in ladles and blast furnaces [76], the estimated power output per square meter rises significantly to approximately 1521.3 W m^{-2}. The calculated power of 1521 W m^{-2} represents a theoretical upper limit based on an ideal ΔT = 800 K and perfect thermal coupling. Actual power output would be lower due to heat losses, contact resistance, and partial surface utilization. This estimate is presented only to illustrate the potential scalability of the SnSe-cement composite under idealized conditions.

Using Equation 3, the final efficiency of said device, assuming a ZT of 0.3, with the same ΔT, an efficiency of ∼5.8% is attainable. This value, though, like the power, should be used as an upper limit estimate.

$$\eta_{\max} = \left(\frac{T_H - T_C}{T_H}\right) * \left(\frac{\sqrt{1+Z\bar{T}} - 1}{\sqrt{1+Z\bar{T}} + \frac{T_C}{T_H}}\right) \quad (3)$$

4 | Conclusion

P-type SnSe-cement slurry composites were created with varying concentrations by weight of cement binder. A simple casting technique was employed, which involved casting this slurry into a silicon mold, and resulted in samples of approximately 1.5 cm^2 by ∼0.75 cm. This technique significantly reduces labor time to manufacture TE materials and has proven to be repeatable. The 0.2% binder concentration sample exhibited the highest power factor of 77 μW m^{-1} K^{-2} at 800 K, with a peak ZT of 0.3 at 850 K was observed in the 0.3% sample at 850 K. A proof-of-concept p-type TEG was also produced, producing a power output of ∼73 μW at 850 K. It was also shown that potentially 1521.3 W m^{-2} of electricity could be harvested from a steel making environment by incorporating these materials into refractories.

Conflicts of Interest

The authors declare no conflict of interest.

Data Availability Statement

The data that support the findings of this study are openly available in Zenodo at 10.5281/zenodo.17143877, reference number 17143877.

References

1. J. Terhaar, T. L. Frölicher, M. T. Aschwanden, P. Friedlingstein, and F. Joos, "Adaptive Emission Reduction Approach To Reach Any Global Warming Target," *Nature Climate Change* 12 (2022): 1136.

2. K. Daehn, R. Basuhi, J. Gregory, M. Berlinger, V. Somjit, and E. A. Olivetti, "Innovations to Decarbonize Materials Industries," *Nature Reviews Materials* 7 (2021): 275, https://doi.org/10.1038/s41578-021-00376-y.

3. G. P. Thiel and A. K. Stark, "To Decarbonize Industry, We Must Decarbonize Heat," *Joule* 5 (2021): 531, https://doi.org/10.1016/j.joule.2020.12.007.

4. J. Wei, L. Yang, Z. Ma, et al., "Review of Current High-ZT Thermoelectric Materials," *Journal of Materials Science* 55 (2020): 12642, https://doi.org/10.1007/s10853-020-04949-0.

5. W. Liu, Q. Jie, H. S. Kim, and Z. Ren, "Current Progress And Future Challenges In Thermoelectric Power Generation: From Materials To Devices," *Acta Materialia* 87 (2015): 357, https://doi.org/10.1016/j.actamat.2014.12.042.

6. L. E. Bell, "Cooling, Heating, Generating Power, and Recovering Waste Heat With Thermoelectric Systems," *Science* 321 (2008): 1457, https://doi.org/10.1126/science.1158899.

7. G. J. Snyder and E. S. Toberer, "Complex Thermoelectric Materials," *Nature Materials* 7 (2008): 105, https://doi.org/10.1038/nmat2090.

8. D. M. Rowe, *Thermoelectrics Handbook: Macro to Nano* (CRC Press, 2005).

9. M. Burton, G. Howells, J. Atoyo, and M. Carnie, "Printed Thermoelectrics," *Advanced Materials* 34 (2022): 2108183, https://doi.org/10.1002/adma.202108183.

10. Joris, *The Potential for Recovering and Using Surplus Heat From Industry Final Report* (Department of Energy & Climate Change, 2014).

11. M. R. Burton, S. Mehraban, J. Mcgettrick, T. Watson, N. P. Lavery, and M. J. Carnie, "Earth Abundant, Non-Toxic, 3D Printed Cu 2−x S With High Thermoelectric Figure of Merit," *Journal of Materials Chemistry A* 7 (2019): 25586, https://doi.org/10.1039/C9TA10064D.

12. M. Massetti, F. Jiao, A. J. Ferguson, et al., "Unconventional Thermoelectric Materials for Energy Harvesting and Sensing Applications," *Chemical Reviews* 121 (2021): 12465, https://doi.org/10.1021/acs.chemrev.1c00218.

13. H. Goldsmid, "Bismuth Telluride and Its Alloys as Materials for Thermoelectric Generation," *Materials* 7 (2014): 2577, https://doi.org/10.3390/ma7042577.

14. O. Yamashita, S. Tomiyoshi, and K. Makita, "Bismuth Telluride Compounds With High Thermoelectric Figures of Merit," *Journal of Applied Physics* 93 (2003): 368, https://doi.org/10.1063/1.1525400.

15. A. Nozariasbmarz, J. S. Krasinski, and D. Vashaee, "N-Type Bismuth Telluride Nanocomposite Materials Optimization for Thermoelectric Generators in Wearable Applications," *Materials* 12 (2019): 1529, https://doi.org/10.3390/ma12091529.

16. F. Shi, C. Tan, H. Wang, et al., "Enhanced Thermoelectric Properties of p-Type Bi 0.48 Sb 1.52 Te 3 /Sb 2 Te 3 Composite," *ACS Applied Materials & Interfaces* 12 (2020): 52922, https://doi.org/10.1021/acsami.0c15991.

17. T. Fu, X. Yue, H. Wu, et al., "Enhanced Thermoelectric Performance of PbTe Bulk Materials with Figure of Merit zT >2 by Multi-Functional Alloying," *Journal of Materiomics* 2 (2016): 141.

18. M. Zebarjadi, K. Esfarjani, M. S. Dresselhaus, Z. F. Ren, and G. Chen, "Perspectives on thermoelectrics: From fundamentals to device applications," *Energy & Environmental Science* 5 (2012): 5147, https://doi.org/10.1039/C1EE02497C.

19. *CRC handbook of chemistry and physics: a ready-reference book of chemical and physical data* (Ed.: D. Lide), (CRC Press, 2005).

20. D. Beretta, N. Neophytou, J. M. Hodges, et al., "Thermoelectrics: From History, a Window to the Future," *Materials Science and Engineering: R: Reports* 138 (2018): 100501, https://doi.org/10.1016/j.mser.2018.09.001.

21. J. O. Morales Ferreiro, D. E. Diaz-Droguett, D. Celentano, et al., "Effect of the Annealing on the Power Factor of Un-Doped Cold-Pressed SnSe,"

Applied Thermal Engineering 111 (2017): 1426, https://doi.org/10.1016/j.applthermaleng.2016.07.198.

22. G. Jeong, Y. H. Jaung, J. Kim, J. Y. Song, and B. Shin, "Sn 1−x Se Thin Films With Low Thermal Conductivity: Role of Stoichiometric Deviation in Thermal Transport," *Journal of Materials Chemistry C* 6 (2018): 10083, https://doi.org/10.1039/C8TC03051K.

23. M. R. Burton, S. Mehraban, D. Beynon, et al., "3D Printed SnSe Thermoelectric Generators With High Figure of Merit," *Advanced Energy Materials* 9 (2019): 1900201, https://doi.org/10.1002/aenm.201900201.

24. M. R. Burton, T. Liu, J. McGettrick, et al., "Thin Film Tin Selenide (SnSe) Thermoelectric Generators Exhibiting Ultralow Thermal Conductivity," *Advanced Materials* 30 (2018): 1801357, https://doi.org/10.1002/adma.201801357.

25. Y. Fu, J. Xu, G. Q. Liu, et al., "Enhanced Thermoelectric Performance in p-Type Polycrystalline SnSe Benefiting From Texture Modulation," *Journal of Materials Chemistry C* 4 (2016): 1201, https://doi.org/10.1039/C5TC03652F.

26. X. Shi, Z. G. Chen, W. Liu, et al., "Achieving High Figure of Merit in P-Type Polycrystalline Sn0.98Se Via Self-Doping and Anisotropy-Strengthening," *Energy Storage Materials* 10 (2018): 130, https://doi.org/10.1016/j.ensm.2017.08.014.

27. N. Xin, Y. Li, G. Tang, and L. Shen, "Enhancing Thermoelectric Performance of K-Doped Polycrystalline SnSe Through Band Engineering Tuning And Hydrogen Reduction," *Journal of Alloys and Compounds* 899 (2022): 163358, https://doi.org/10.1016/j.jallcom.2021.163358.

28. Y. K. Lee, Z. Luo, S. P. Cho, M. G. Kanatzidis, and I. Chung, "Surface Oxide Removal for Polycrystalline SnSe Reveals Near-Single-Crystal Thermoelectric Performance," *Joule* 3 (2019): 719, https://doi.org/10.1016/j.joule.2019.01.001.

29. Y. Gong, C. Chang, W. Wei, et al., "Extremely Low Thermal Conductivity and Enhanced Thermoelectric Performance of Polycrystalline SnSe by Cu Doping," *Scripta Materialia* 147 (2018): 74, https://doi.org/10.1016/j.scriptamat.2017.12.035.

30. S. Sassi, C. Candolfi, J. B. Vaney, et al., "Assessment of the Thermoelectric Performance of Polycrystalline p -type SnSe," *Applied Physics Letters* 104 (2014): 212105, https://doi.org/10.1063/1.4880817.

31. E. K. Chere, Q. Zhang, K. Dahal, F. Cao, J. Mao, and Z. Ren, "Studies on Thermoelectric Figure of Merit of Na-Doped p-Type Polycrystalline SnSe," *Journal of Materials Chemistry A* 4 (2016): 1848, https://doi.org/10.1039/C5TA08847J.

32. C. L. Chen, H. Wang, Y. Y. Chen, T. Day, and G. J. Snyder, "Thermoelectric Properties of p-Type Polycrystalline SnSe doped With Ag," *Journal of Materials Chemistry A* 2 (2014): 11171, https://doi.org/10.1039/C4TA01643B.

33. Y. Li, X. Shi, D. Ren, J. Chen, and L. Chen, "Investigation of the Anisotropic Thermoelectric Properties of Oriented Polycrystalline SnSe," *Energies* 8 (2015): 6275, https://doi.org/10.3390/en8076275.

34. X. Shi, A. Wu, W. Liu, et al., "Polycrystalline SnSe With Extraordinary Thermoelectric Property via Nanoporous Design," *ACS Nano* 12 (2018): 11417, https://doi.org/10.1021/acsnano.8b06387.

35. Y. Li, F. Li, J. Dong, et al., "Enhanced Mid-Temperature Thermoelectric Performance of Textured SnSe Polycrystals Made of Solvothermally Synthesized Powders," *Journal of Materials Chemistry C* 4 (2016): 2047–2055.

36. S. Hou, Z. Li, Y. Xue, X. Ning, J. Wang, and S. Wang, "Surprisingly High In-Plane Thermoelectric Performance in A-Axis-Oriented Epitaxial SnSe Thin Films," *Materials Today Physics* 18 (2021): 100399.

37. H. S. Kim, Z. M. Gibbs, Y. Tang, H. Wang, and G. J. Snyder, "Characterization of Lorenz Number with Seebeck Coefficient Measurement," *APL Materials* 3 (2015): 041506.

38. L. D. Zhao, S. H. Lo, Y. Zhang, et al., "Ultralow thermal conductivity and high thermoelectric figure of merit in SnSe crystals," *Nature* 508 (2014): 373, https://doi.org/10.1038/nature13184.

39. C. Zhou, Y. K. Lee, Y. Yu, et al., "Polycrystalline SnSe With a Thermoelectric Figure of Merit Greater Than the single Crystal," *Nature Materials* 20 (2021): 1378, https://doi.org/10.1038/s41563-021-01064-6.

40. M. Jin, J. Jiang, R. Li, et al., "Growth of Large size SnSe Single Crystal and Comparison of its Thermoelectric Property With Polycrystal," *Materials Research Bulletin* 114 (2019): 156, https://doi.org/10.1016/j.materresbull.2019.02.024.

41. F. O. Faisal, K. Singsoog, S. M. Melania, and T. Seetawan, *Journal of Physics:Conference Series* (2020): 1428, https://doi.org/10.1088/1742-6596/1428/1/012007.

42. K. Yazawa and A. Shakouri, "Cost-Performance Analysis and Optimization of Fuel-Burning Thermoelectric Power Generators," *Journal of Electronic Materials* 42 (2013): 1946.

43. Z. Cao, M. J. Tudor, R. N. Torah, and S. P. Beeby, "Screen Printable Flexible BiTe–SbTe-Based Composite Thermoelectric Materials on Textiles for Wearable Applications," *IEEE Transactions on Electron Devices* 63 (2016): 4024, https://doi.org/10.1109/TED.2016.2603071.

44. C. Han, G. Tan, T. Varghese, M. G. Kanatzidis, and Y. Zhang, "High-Performance PbTe Thermoelectric Films by Scalable and Low-Cost Printing," *ACS Energy Letters* 3 (2018): 818, https://doi.org/10.1021/acsenergylett.8b00041.

45. B. Chen, M. Kruse, B. Xu, et al., "Flexible Thermoelectric Generators With Inkjet-Printed Bismuth Telluride Nanowires and Liquid Metal Contacts," *Nanoscale* 11 (2019): 5222, https://doi.org/10.1039/C8NR09101C.

46. Z. Cao, J. J. Shi, R. N. Torah, M. J. Tudor, and S. P. Beeby, "All Dispenser Printed Flexible 3D Structured Thermoelectric Generators," *Journal of Physics: Conference Series* 660 (2015): 012096, https://doi.org/10.1088/1742-6596/660/1/012096.

47. D. Madan, A. Chen, P. K. Wright, and J. W. Evans, "Dispenser Printed Composite Thermoelectric Thick Films For Thermoelectric Generator Applications," *Journal of Applied Physics* 109 (2011): 034904, https://doi.org/10.1063/1.3544501.

48. A. Chen, D. Madan, P. K. Wright, and J. W. Evans, "Dispenser-Printed Planar Thick-Film Thermoelectric Energy Generators," *Journal of Micromechanics and Microengineering* 21 (2011): 104006, https://doi.org/10.1088/0960-1317/21/10/104006.

49. P. C. Aïtcin, "6 - Entrained Air in Concrete: Rheology and Freezing Resistance," *Science and Technology of Concrete Admixtures* (2016): 27.

50. J. Wei, L. Zhao, Q. Zhang, Z. Nie, and L. Hao, "Enhanced Thermoelectric Properties Of Cement-Based Composites With Expanded Graphite For Climate Adaptation And Large-Scale Energy Harvesting," *Energy and Buildings* 159 (2018): 66, https://doi.org/10.1016/j.enbuild.2017.10.032.

51. J. Wei, Z. Nie, G. He, L. Hao, L. Zhao, and Q. Zhang, "Energy Harvesting From Solar Irradiation In Cities Using The Thermoelectric Behavior Of Carbon Fiber Reinforced Cement Composites," *RSC Advances* 4 (2014): 48128.

52. J. Wei, Y. Fan, L. Zhao, F. Xue, L. Hao, and Q. Zhang, "Thermoelectric Properties Of Carbon Nanotube Reinforced Cement-Based Composites Fabricated By Compression Shear," *Ceramics International* 44 (2018): 5829–5833, https://doi.org/10.1016/j.ceramint.2018.01.074.

53. S. Ghosh, S. Harish, K. A. Rocky, M. Ohtaki, and B. B. Saha, "Graphene Enhanced Thermoelectric Properties Of Cement Based Composites For Building Energy Harvesting," *Energy and Buildings* 202 (2019): 109419, https://doi.org/10.1016/j.enbuild.2019.109419.

54. J. Wei, Q. Zhang, L. Zhao, L. Hao, and C. Yang, "Enhanced Thermoelectric Properties Of Carbon Fiber Reinforced Cement Composites," *Ceramics International* 42 (2016): 11568–11573, https://doi.org/10.1016/j.ceramint.2016.04.014.

55. T. Ji, X. Zhang, X. Zhang, Y. Zhang, and W. Li, "Effect of Manganese Dioxide Nanorods on the Thermoelectric Properties of Cement Com-

posites," *Journal of Materials in Civil Engineering* 30 (2018): 04018224, https://doi.org/10.1061/(ASCE)MT.1943-5533.0002401.

56. H. Cao, W. Yao, and J. Qin, "Seebeck Effect In Graphite-Carbon Fiber Cement Based Composite," *Advances in Materials Research* 177 (2011): 566–569.

57. B. Demirel and S. Yazicioglu, "Thermoelectric Behavior Of Carbon Fiber Reinforced Lightweight Concrete With Mineral Admixtures," *New Carbon Materials* 23 (2008): 21.

58. J. Zuo, W. Yao, and K. Wu, "Seebeck Effect and Mechanical Properties of Carbon Nanotube-Carbon Fiber/Cement Nanocomposites," *Fullerenes, Nanotubes and Carbon Nanostructures* 23 (2014): 383, https://doi.org/10.1080/1536383X.2013.863760.

59. S. Ghosh, S. Harish, M. Ohtaki, and B. B. Saha, "Enhanced Figure of Merit of Cement Composites with Graphene and ZnO Nanoinclusions for Efficient Energy Harvesting in Buildings," *Energy* 198 (2020): 117396, https://doi.org/10.1016/j.energy.2020.117396.

60. J. Wei, Y. Wang, X. Li, et al., "Dramatically Improved Thermoelectric Properties by Defect Engineering in Cement-Based Composites," *ACS Applied Materials & Interfaces* 13 (2021): 3919, https://doi.org/10.1021/acsami.0c18863.

61. G. Howells, S. Mehraban, J. McGettrick, N. Lavery, M. J. Carnie, and M. Burton, "Rapid Printing of Pseudo-3D Printed SnSe Thermoelectric Generators Utilizing an Inorganic Binder," *ACS Appl Mater Interfaces* (2023), https://doi.org/10.1021/ACSAMI.3C01209.

62. T. R. Wei, M. Guan, J. Yu, T. Zhu, L. Chen, and X. Shi, "How to Measure Thermoelectric Properties Reliably," *Joule* 2 (2018): 2183, https://doi.org/10.1016/j.joule.2018.10.020.

63. Z. Zainal, S. Nagalingam, A. Kassim, M. Z. Hussein, and W. M. M. Yunus, "Effects of Annealing on the Properties of SnSe Films," *Solar Energy Materials and Solar Cells* 81 (2004): 261, https://doi.org/10.1016/j.solmat.2003.11.004.

64. H. Yu, S. Dai, and Y. Chen, "Enhanced Power Factor via the Control of Structural Phase Transition in SnSe," *Reports* 6 (2016): 1.

65. G. Tang, J. Liu, J. Zhang, et al., "Realizing High Thermoelectric Performance Below Phase Transition Temperature In Polycrystalline SnSe Via Lattice Anharmonicity Strengthening And Strain Engineering," *ACS Applied Materials and Interfaces* 10 (2018): 30558.

66. S. Wen and D. D. L. Chung.

67. L. Tzounis, M. Liebscher, R. Fuge, A. Leonhardt, and V. Mechtcherine, "P- and n-type thermoelectric cement composites With CVD grown p- and n-doped carbon nanotubes: Demonstration of a structural thermoelectric generator," *Energy and Buildings* 191 (2019): 151, https://doi.org/10.1016/j.enbuild.2019.03.027.

68. S. Wen and D. D. L. Chung *Cement and Concrete Research* 1999 (1989).

69. Y. Cui and Y. Wei, "Mixed "ionic-electronic" thermoelectric effect of reduced graphene oxide reinforced cement-based composites," *Cement and Concrete Composites* 128 (2022): 104442, https://doi.org/10.1016/j.cemconcomp.2022.104442.

70. M. Shi, J. Han, and D. Zhang, "Insight Into the ionic thermoelectric effect and electrochemical energy storage of Portland cement," *Construction and Building Materials* 500 (2025): 144173, https://doi.org/10.1016/j.conbuildmat.2025.144173.

71. Y. Wei, Y. Cui, and Y. Wang, "Ionic thermoelectric effect of pure cement paste and its temperature sensing performance," *Construction and Building Materials* 364 (2023): 129898, https://doi.org/10.1016/j.conbuildmat.2022.129898.

72. P. Fan, Z. H. Zheng, Y. Z. Li, et al., "Low-cost flexible thin film thermoelectric generator on zinc based thermoelectric materials," *Applied Physics Letters* 106 (2015): 073901, https://doi.org/10.1063/1.4909531.

73. V. Semenyuk, "Effect of Electrical Contact Resistance on the Performance of Cascade Thermoelectric Coolers," *Journal of Electronic Materials* 48 (2019): 1870, https://doi.org/10.1007/s11664-018-6785-5.

74. Y. Xing, K. Tang, J. Wang, et al., "High-Performance Wearable Bi2Te3-Based Thermoelectric Generator," *Applied Sciences* 13 (2023): 5971.

75. P. Brinks and M. Huijben *Ep Growth Complex Metal Oxides* (2015): 397.

76. L. Cotton *Thermal Measurement and Degradation Quantification of Teeming Ladle Refractories and the Effects on the Process*, (Swansea University, 2021).

Supporting Information

Additional supporting information can be found online in the Supporting Information section.

Supporting file: aelm70229-sup-0001-SuppMat.pdf